3. THE IMPACT OF CATHODE – ANODE GAP ON ELECTRON EMISSION AT ATMOSPHERIC PRESSURE

3.1 Background and Motivation

Electronic device manufacturing continues to demand reduced device sizes, necessitating characterization of gas breakdown for these devices[2,73]. The application of these devices in the medical, aerospace, and consumer electronics further accelerates size reductions[9,15,22,23,74]. Recent work has laid the ground work for better understanding of gas breakdown by examining the effects of removing material dependence in breakdown theory by creating scaling laws[31]. Modern work predicting breakdown relies on empirical constants that have been measured at limited conditions. The scaling laws developed helped to create a universal theory of breakdown that removed material dependence for microscale field emission (FE) discharges and discharges created by Townsend avalanche that follow the classical Paschen's Law (PL) [26]. Further exploring the FE effects at microscale work showed that Townsend avalanche was insufficiently strong to induce a sustained avalanche for sufficiently small gaps, meaning that FE driven breakdown drove breakdown[72].

The importance of FE in microscale gas breakdown naturally leads to the question concerning other electron emission mechanisms. Theory, simulation, and experiment indicate that electron emission transitions from FE, as defined by the Fowler-Nordheim law, to space-charge limited emission, as defined by the Child-Langmuir law, as one reduced diode size at vacuum. At even smaller gap sizes, one transitions from the classical Child-Langmuir law to the quantum space-charge limited law.

This dissertation's focus on atmospheric pressure raises the question about how electron emission transitions with reducing gap size when pressure is included. Another graduate student in the group is currently unifying space charge limited breakdown, Child-Langmuir (CL) and Mott-Gurney (MG), which is space-charge limited emission with collisions, FN, and PL[75] . This model is universal (true for any gas) except or a single material-dependent constant in PL. An intermediate step performed by another graduate student in our research group unified CL, MG, and FE[54]; this student has expanded this concept to unify CL, MG, FE, Ohm's law (for an external resistor), and thermionic emission[76]. Unification of these theories moves closer to providing experimentalists a guideline for selecting device parameters to satisfy desired emission conditions or avoid/create breakdown *a priori*. Although these approaches are generally for perfectly smooth

electrodes, surface roughness can cause field enhancement, which may modify the predictions above. [77]

Experimental work exploring electron emission for nanoscale diodes characterized the transition from field emission to quantum space-charge limited emission and classical space-charge limited emission at vacuum[51,78]. For the smallest gaps, comparable to the de Broglie wavelength of the electrons, $I \propto V^{1/2}$, indicating quantum space charge limited emission current scaling [79–81]. Further work explored the effects of microscale repetitive discharges on a pin to plate configuration quantifying the transition from field emission of electrons to the self-sustained plasma breakdown of the gap[68]. Microscale gaps on the micro-scale field emission current had negligible impact on the pre-breakdown regime of the discharge. To further explore the effects on the microscale work was done expanding the pin to plate geometry to look at how repetitive breakdown events altered the breakdown condition[82]. Repetitive breakdown events significantly altered the surface structure of the electrodes, leading to altered gap distance significantly larger than the initial conditions. The altered surface structure affects sharp or blunt nanoscale features, potentially modifying the field enhancement on the surface, leading to an altered effective work function. The effects of these sharp and blunt features were the focus of theoretical formulations studying emission physics in nanoscale diodes[67]. The width, height, and degree of sharpness of individual nanostructures significantly impacts the emission physics of a nanoscale gap DC device.

This chapter expands upon the theoretical work to measure the emission current from the nanoscale devices. The devices are based on the geometry from Lin, et al. in 2017[67]. The nano-scale devices were fabricated at Birck Nanotechnology Center at Purdue University, and testing was conducted to measure electron emission current as applied voltage was increased. The measured current allows for determination of emission regime along with estimates for emission area and electron mobility. The measured currents were also evaluated in terms of previous theoretical work showing transitions between the regimes

3.2   Materials and Methods

Lin, et al. theoretically examined the implications of electrode geometry on emission current for nanoscale diodes[67]. We used this geometry as a baseline for designing devices for assessing gas breakdown and electron emission for various gap distances and electrode aspect

ratios. The tests were conducted in air at atmospheric pressure to simulate typical usage in modern electronics.

Figure 3.1 shows the geometry used to fabricate the test devices. Each device consists of two 100 μm square test pads separated by a gap d. One of the test pads is smooth; the second has a surface protrusion of length h, width $2a$, and angle α. We fixed $\alpha = 45°$ and constructed devices with various h and a. Adjusting h for a fixed a varied both the effective interelectrode gap distance $d_{eff} = d\text{-}h$ and changed protrusion's aspect ratio; adjusting a just changed the aspect ratio. The test pads were fabricated directly onto the design of the devices by making 100 μm × 100 μm squares on each side. The pads were used to place test probe electrodes onto the devices to apply voltage and measure current.
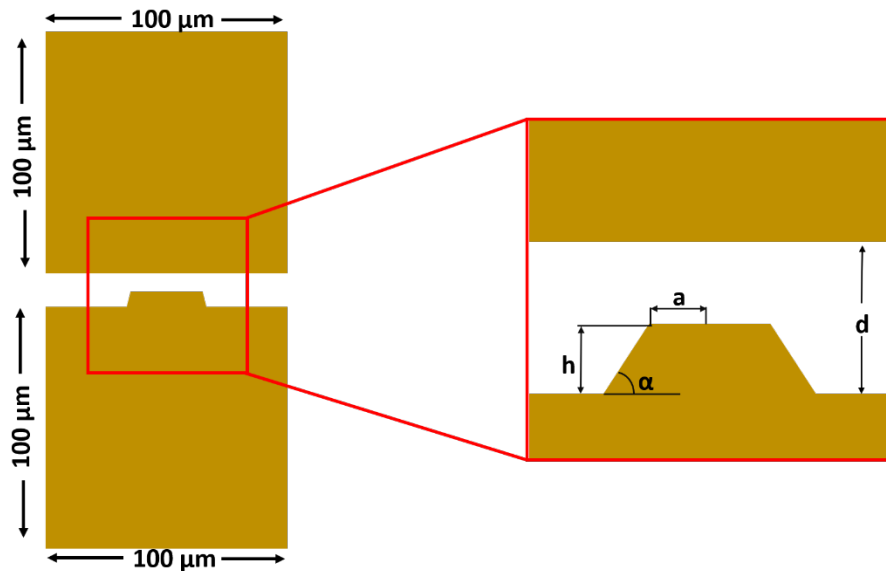

Figure 3.1: Geometry of the designed nanoscale device showing the sharp or blunt surface protrusion to evaluate field enhancement through current emission measurement and scaling by altering a, h, and d and fixing α.

Birck Nanotechnology Center fabricated these devices using electron beam lithography (EBL) on a base silicon wafer with a top layer of silicon dioxide to ensure electrical insulation of the devices. Multiple devices were fabricated on a single wafer per run to provide multiple devices for testing. Devices were then created on top of the electrically insulative layer using 5 nm of titanium and 100 nm of gold. Figure 3.2 shows the layers as they were produced along with cross-section and top views of the devices.
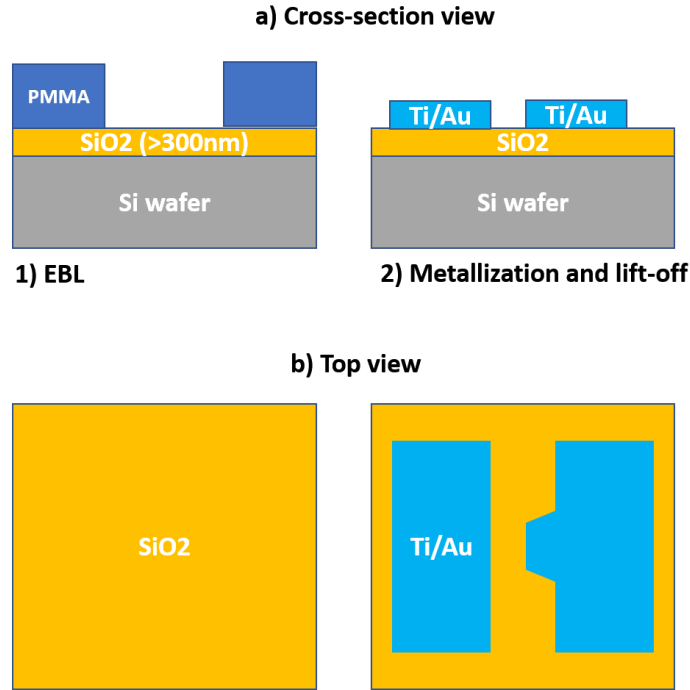
Figure 3.2: (a) The cross-section of the fabrication process showing the poly-methyl methacrylate (PMMA) photo-resist layer with an electrical insulation layer of SiO2, and an electrode layer of 5 nm of titanium under a 100 nm layer of gold. (b) shows the general shape of the devices considered before the 100 μm pads are added to the design to facilitate testing.

Following the process described above and the general layering shown in Figure 3.2, we fabricated 200 devices per chip consisting of five replicates of forty different variations of the protrusion with different d, h, a, and $d_{eff} = d - h$. Table 3.1 lists the parameter space of the designs in its entirety.

Table 3.1: Parameter space used to fabricate devices.

Data #	a [nm]	h [nm]	d [nm]	$d_{eff} = d - h$ [nm]
1	384	769	1000	230
2	76	769	1000	230
3	38	769	1000	230
4	192	769	1000	230
5	769	769	1000	230
6	50	500	1000	500
7	125	500	1000	500
8	250	500	1000	500
9	500	500	1000	500
10	62	250	1000	750
11	125	250	1000	750
12	250	250	1000	750
13	100	50	1000	950
14	100	100	1000	900
15	38	384	500	115
16	96	354	500	145
17	192	384	500	115
18	384	384	500	115
19	62	250	500	250
20	125	250	500	250

Table 3.1 Continued: Parameter space used to fabricate devices.

Data #	a [nm]	h [nm]	d [nm]	$d_{eff} = d - h$ [nm]
21	250	250	500	250
22	31	125	500	375
23	62	125	500	375
24	125	125	500	375
25	25	50	500	450
26	50	50	500	450
27	48	192	250	57
28	31	125	250	125
29	96	192	250	57
30	62	125	250	125
31	31	62	250	187
32	25	25	250	225
33	192	192	250	57
34	125	124	250	126
35	62	62	250	187
36	48	96	125	28
37	62	62	125	62
38	96	96	125	28
39	31	62	125	62
40	31	31	125	93

The edge of each device was 400 µm away from its nearest neighbor to minimize electromagnetic interference during testing. Due to the solid-state design and voltages applied heating issues were not able to be mitigated for these tests. Figure 3.3 shows the layout of each chip, with a blown-up view showing labeling of each device on the chip. The blown-up view in Figure 3.3(b) shows the orientation of the devices on the chip with the protrusion always on the bottom pad, protruding into the middle of the device. The gap is too small to be seen in these images.
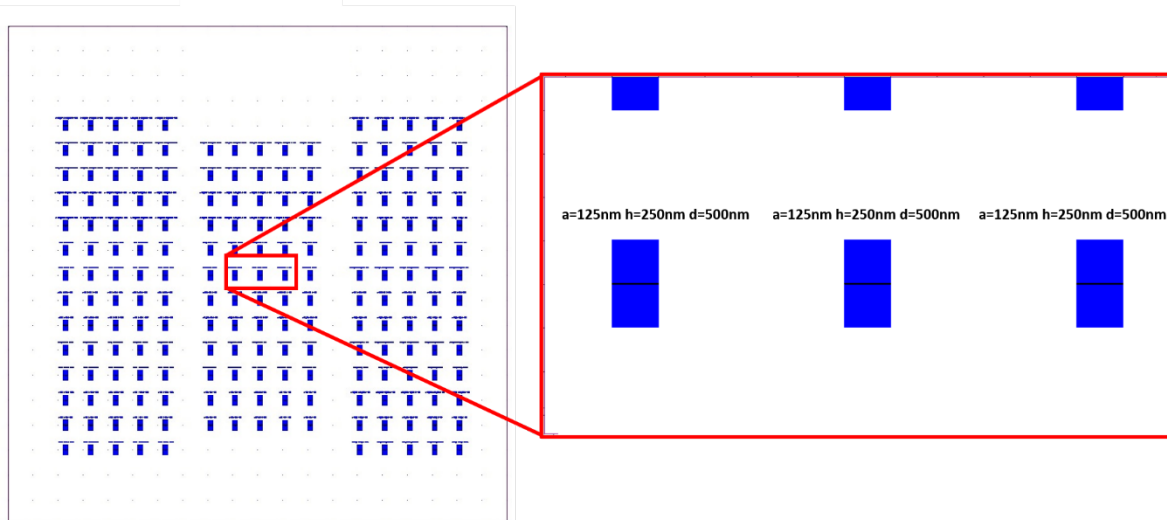
Figure 3.3: Layout of devices on 1 cm × 1 cm square chips cut from silicon wafer with a view of the device layout showing spacing for testing.

We measured the emitted current as a function of applied voltage using a Keithley 2410-C source meter unit (SMU) with sensing current sensitivity of 1 nA and sourcing voltage with a resolution of 1 µV. The measured current was based on a two wire reverse bias diode test with current measured at a user specified rate during a voltage sweep[83]. We used the microscope and micromanipulators present on the Signatone H-150W DC probe station to place tungsten PTT 12/4-25 needle probes with tips with a diameter of 1.2 µm on each of the gold test pads fabricated on the devices. The positive probe was always placed on the pad with the protrusion feature for each test. The test consisted of a voltage sweep starting at 0 V with steps of 0.005 V lasting 0.1 s until the current spiked, indicating device failure and melting, with current sampled at 10 samples per second. Device failure was confirmed by using a microscope to confirm test pad degradation. Figure 3.4 shows the general electrical test setup as it was connected to each device.
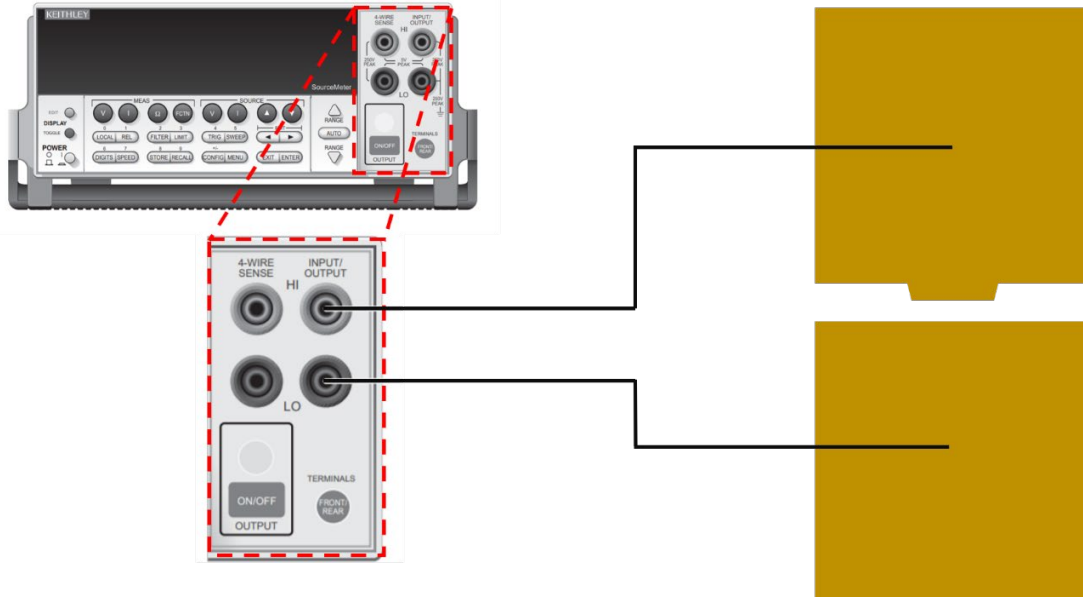
Figure 3.4: Electrical testing setup of the Keithley 2410C source meter unit (SMU) to apply voltage and measure current across the test devices[84].

3.3 Results

Using previously published methods, the data was analyzed to determine which emission regime the devices were during the test[51,68,78]. Current (amperes) and voltage (volts) data was collected during the test and plotted with different fits and axes scaling to observe regions that are linear. The current density J for the different emission regimes of interest, the classical Child-Langmuir law (CL), Fowler-Nordheim (FN) law, and Mott-Gurney (MG) law, may be written as

$$J_{CL} = \frac{4\varepsilon_0}{9}\left(\frac{2e}{m}\right)^{1/2}\frac{V^{3/2}}{d^2}, \tag{3.1}$$

$$J_{FN} = A_{FN}(\beta V)^2 \exp\left[\frac{-B_{FN}\phi_w^{3/2}}{\beta V}\right], \tag{3.2}$$

and

$$J_{MG} = \frac{9}{8}\varepsilon\mu\frac{V^2}{d^3}, \tag{3.3}$$

respectively, where e is electron charge, ε_0 is the permittivity of free space, m is electron mass, V is applied voltage, $d_{eff} = d - h$ is the effective gap distance from the protrusion to the flat electrode, A_{FN} and B_{FN} are Fowler-Nordheim constants, ϕ_w is the electrode work function, ε is the permittivity of the medium, and μ is the electron mobility[43,50,85]. Thus, plotting experimentally measured I (since $J = I/A$, where A is the emission area, is not known *a priori*) as a function of V

can provide insight into the appropriate mechanism based on the functional relationships. In other words, $I \propto V^{3/2}$ denotes CL, $I \propto V^2$ denotes MG, and $\ln(I/V^2) \propto V^{-1}$ gives FN (known as a "FN curve"). Theoretical assessments indicate that these simple scaling relationships strictly hold only in the asymptotic limits of high μ and/or high V for CL, low μ for MG, and low V for FN[54,77]; intermediate levels require an exact solution of the full force law for an electron emitted from the cathode, leading to measured I that falls between the various asymptotic limits[54,77].

We first plotted the data on a FN curve since we anticipate FN scaling at low V. Figure 3.5 shows the FN curves for (a) $a = 192$ nm $\pm$ 10 nm with three values of d_{eff} and (b) $d_{eff} = 115$ nm $\pm$ 10 nm and three different a values.
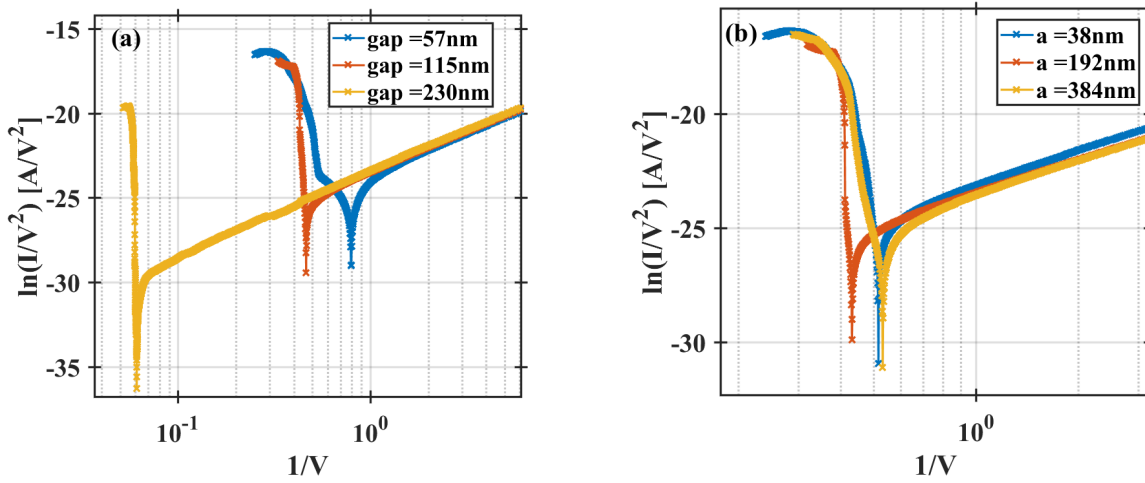
Figure 3.5: FN scaling of the data for (a) with $a = 192$ nm $\pm$ 10 nm and $d_{eff} = 57$ nm $\pm$ 10 nm, 115 nm $\pm$ 10 nm, and 230 nm $\pm$ 10 nm and (b) with $d_{eff} = 115$ nm $\pm$ 10 nm and $a = $ 38 nm $\pm$ 10 nm, 192.3077 nm $\pm$ 10 nm, and 384 nm $\pm$ 10 nm showing strong gap dependence on breakdown voltage but no dependence on width $2a$.

Figure 3.5 shows that the effective gap size of $d_{eff} = d - h$ has a dominant effect on the emission current and breakdown of the device. Breakdown was determined by a sudden spike in current, leading directly to a constant current value that indicated a short circuit, or device failure. A dramatic change in slope from the FN regime occurred during breakdown. Device shorting was confirmed with the microscope as visible damage to the devices from heating was observed. Figure 3.5(a) shows that the breakdown voltage increases with increasing d_{eff} while Figure 3.5(b) shows that it is insensitive to changes in a. Table 3.2 shows the estimated breakdown voltage (V_{BD}) for each of the cases presented in Figure 3.5.

Table 3.2: Estimated breakdown voltage from FN plots for each case presented.

$d_{eff} = d - h$ [nm]	a [nm]	V_{BD} [nV]
57	192	1.9
115	192	2.3
230	192	16.7
115	38	2.1
115	192	2.0
115	384	2.4

Table 3.2 shows that V_{BD} generally increased with increasing d_{eff} and that a did not have any particular effect. The linear region on the FN curve indicate the regime where FN emission dominates. We performed a linear regression over this region to fit the Fowler-Nordheim constants A_{FN} and B_{FN} for each case. The emission area and mobility were estimated using a least squares fit to obtain the current density J. This process permits comparison of the experimental data to the theory describing the transition between the regimes[54]. Since emission area and mobility are unknown, we can only set limits, varying both until experiment and theory have notably deviated setting an upper limit for the data. Due to the design of the parameter space, not all gap distances were fabricated for each feature width a, resulting in different d_{eff} being used for the data presented in some cases. For the smallest mobility considered, Figure 3.6 shows $d_{eff} = 28$ nm $\pm$ 10 nm and a fitted emission area of 64 nm^2. Regardless of the mobility used, emission current is clearly FN dominated until breakdown conditions are reached.
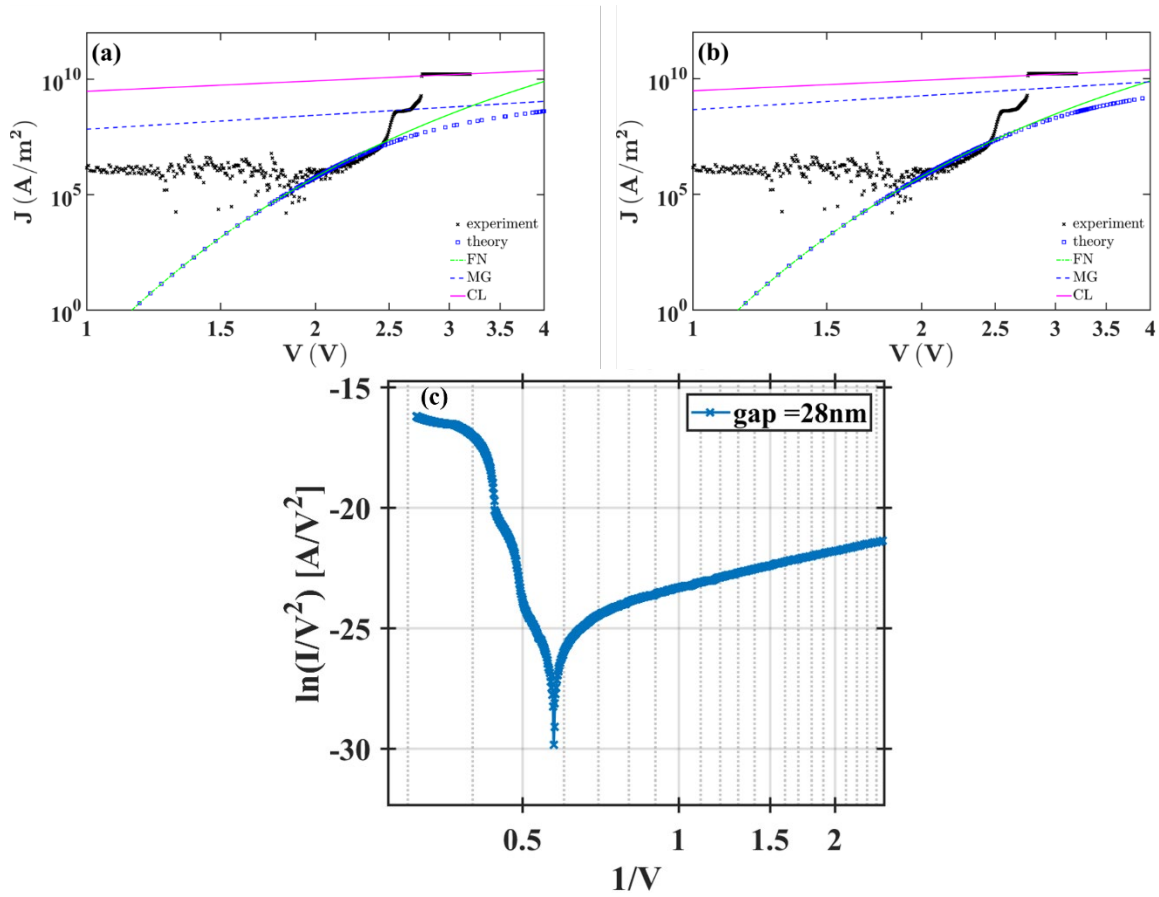
Figure 3.6: Experimental data for d_{eff} = 28 nm ± 10 nm and a fitted emission area of 64 nm² fit to full theory from Darr, et. al. using mobility of (a) 0.00015 m²V⁻¹s⁻¹ and (b) 0.001 m²V⁻¹s⁻¹showing FN dominated emission transitioning to breakdown as the device fails and (c) the associated FN plot for Ref. [54].

For d_{eff} = 28 nm ± 10 nm and a fitted emission area of 64 nm² fit to full theory from Darr et. al. using mobility of (a) 0.00015 m²V⁻¹s⁻¹ and (b) 0.001 m²V⁻¹s⁻¹ showing fieldemission transitioning to breakdown as the device fails and (c) the associated FN plot for Ref [54]. The plateau regions that appear to scale with MG or CL emission are attributed to the physical deterioration of the device during the test because they occur after a large spike in current and cannot be explained by either theory. Viewing the devices under the microscope showed that the devices heated to the point of melting during the test, which contributed to the direct transition to breakdown and accounts for the constant current value at the higher applied voltages.

As gap size is increased the transition behavior predicted by Darr, et al. is observed in the data[54]. Figure 3.7 shows the transition behavior for a d_{eff} = 125 nm ± 10 nm and a fitted emission

71

area of 64 nm^2 with mobilities of (a) 0.0003 m^{2}V^{-1}s^{-1}and (b) 0.001 m^{2}V^{-1}s^{-1}. It is assumed that the lower mobility causes the data to approach the MG asymptote; however, the exact theoretical model poorly predicts the experimental data for this mobility. Using higher mobility (cf. Figure 3.7 (b)) gives better agreement between the exact solution[54] and the experimental data, suggesting that it is more representative of the data. In this case, the measured current follows FN at lower current and space charge just begins to contribute prior to breakdown. The testing of the devices was halted as the breakdown was observed. Note that the emission is transitioning to space-charge dominated because the experimental results and the exact solution still do not approach the MG asymptote.
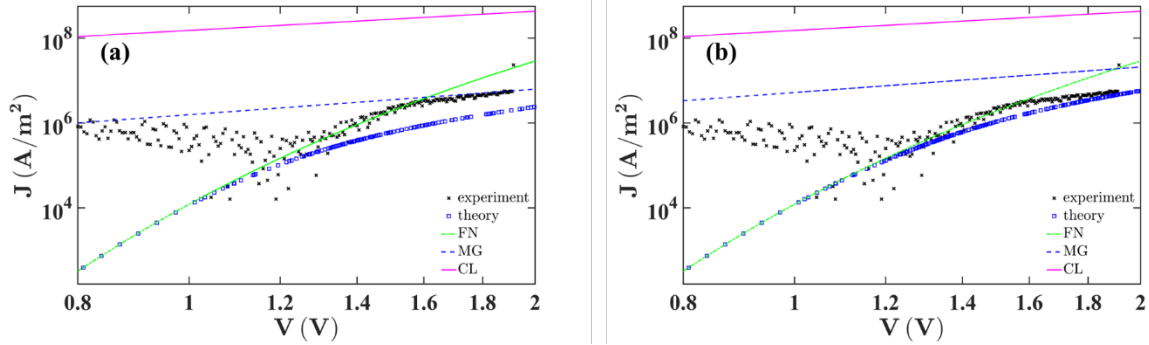

Figure 3.7: Transition behavior for d_{eff} = 125 nm ± 10 nm using mobilities of (a) 0.0003 m^{2}V^{-1}s^{-1} and (b) 0.001 m^{2}V^{-1}s^{-1}. Using the lower mobility predicts transition to MG; however, the full theory does not match the experimental data. The higher mobility agrees better with the experimental results and indicates that the data primarily follows FN over this regime.

Figure 3.8 repeats this process for d_{eff} = 450 nm ± 10 nm and a fitted emission area of 64 nm^2 with mobilities of (a) 0.003 m^{2}V^{-1}s^{-1}and (b) 0.01 m^{2}V^{-1}s^{-1}. In this case, the exact solution, the FN asymptote, and the experimental data all match prior to breakdown occurring, as indicated by the spike in current. Thus, as with conventional microscale gas breakdown and d_{eff} = 28 nm, breakdown directly occurs from field emission.

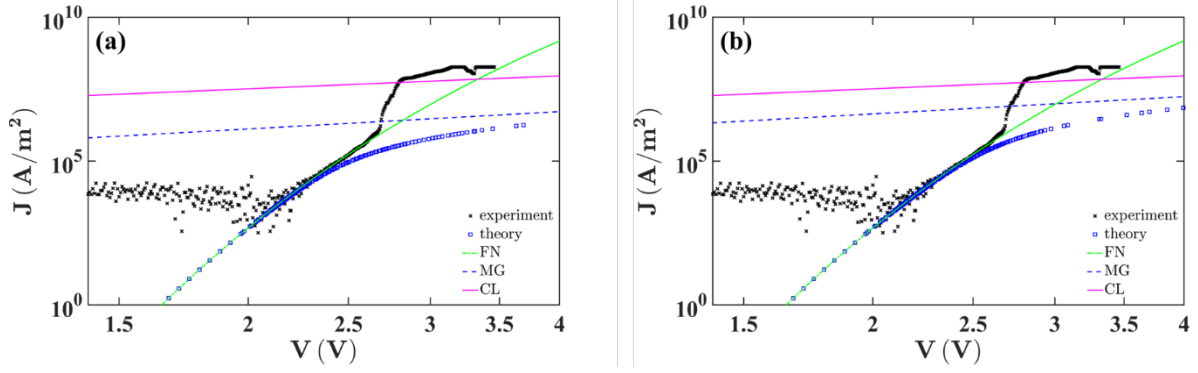Figure 3.8: JV plot for a device with d_{eff} of 450 nm ± 10 nm and a fitted emission area of 64 nm^2 with mobilities of (a) 0.003 m^{2}V^{-1}s^{-1} and (b) 0.01 m^{2}V^{-1}s^{-1} showing no transition behavior, moving directly from FN dominant emission to breakdown.

Figure 3.6 - Figure 3.8 show that emission transitions from FN toward MG without transitioning directly to breakdown only for $d_{eff} \approx$ 125 nm. Breakdown is observed due to the almost vertical spike in current density at high V rather than following the full solution emission curve. To understand why, we equate the asymptotic solutions from (3.2) and (3.3) to obtain

$$V_{FN-MG} = B_{FN}D / \ln\left(\frac{8A_{FN}d_{eff}}{9\mu\epsilon_0}\right) \tag{3.4}$$

which has a minimum at

$$d_{eff} = 9\mu\varepsilon_0 \exp(1) / 8A_{FN}. \tag{3.5}$$

To examine the relevance of this behavior on the transition from field emission to space-charge limited emission, and its effect on the data presented (3.4) was plotted for d_{eff}= 28 nm case with μ = 0.00299 m^{2}V^{-1}s^{-1} , A = 6.4×10^{17} m^2, A_{FN} = 0.0013 A·eV·V^{-2}, and B_{FN} = 1.1645×10^9 Vcm^{-1}eV$^{-3/2}$ found from fitting (3.2) to the experimental data.
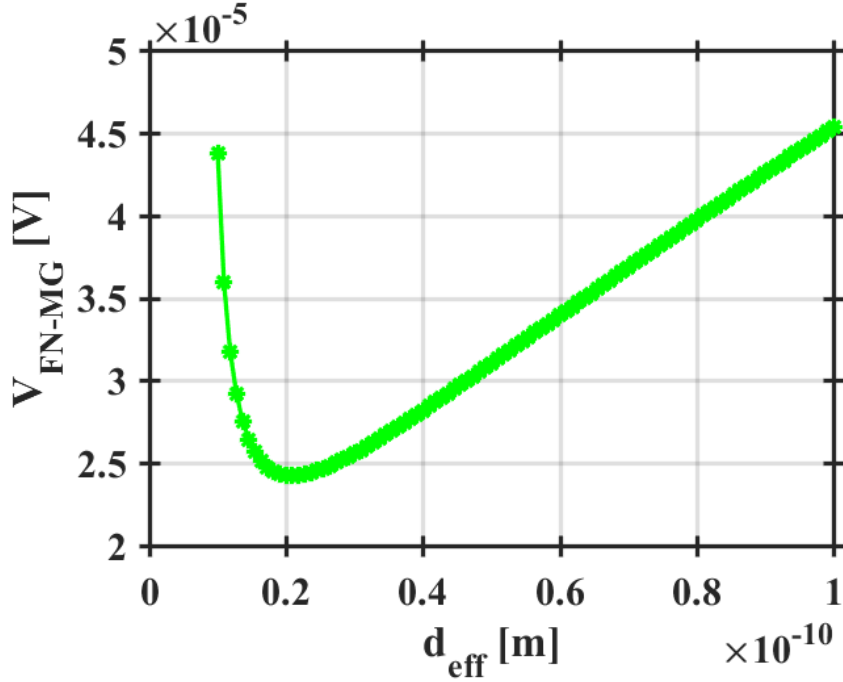
Figure 3.9: Transition voltage presented from (3.4) for μ =0.00299 m^{2}V^{-1}s^{-1} , A= 6.4×1017 m^2, A_{FN} = 0.0013 AeV $\cdot$ V^{-2}, and B_{FN} =1.1645×10^9 Vcm^{-1}eV$^{-3/2}$ demonstrating that the minimum voltage for the transition from FN to MG to occur is for $d_{eff} \approx$ 0.02 nm.

Figure 3.9 should be considered as a representative curve useful for analyzing devices with known FN and mobility parameters. This implies that there is a specific gap distance for which the transition will occur. The device was operating at a voltage clearly on the far-right side of the curve shown, meaning it was not near a transition condition of gap and applied voltage. This may explain the presence of the transition behavior shown in the 125 nm ± 10 nm data but not in either the 28 nm ± 10 nm or the 450 nm ± 10 nm. Since the calculated mobility and FN constants are fit from the data, this should be considered as an estimate as we cannot directly measure them for the devices tested. Table 3.3 shows the upper limit estimates of the mobility μ, area A, and relative error σ comparing the current to the FN solution assuming the largest possible emission area for the three d_{eff} considered.

Table 3.3: Summary of upper limit estimates for mobility μ, area A, and the resulting relative error σ between the current and the FN current for the three different gap distances considered.

d_{eff} [nm]	A [nm^2]	μ [m^{2}V^{-1}s^{-1}]	σ
28	95.101504	0.00299	0.0994
125	59.954049	0.0162	0.1054
450	905542.56	0.0483	0.081

Table 3.3 shows that the emission area increases dramatically with gap distance. The limits for μ and A are based on σ obtained from the least squares fit of the data to the full theoretical solution assuming an arbitrarily large emission area. This serves as a scale for the minimum error possible for the data in the sets fit. The calculated A and μ assumed 30% as the maximum error when presenting the data in the previous figures. The largest estimated area is about 0.9 μm^2, which is still about 10 times smaller than the actual total area of the device. The total possible emission area would occur if the entire gap emitted electrons from the test pad edges that are 100 μm long and 105 nm tall. Despite this increased emission area, the larger gaps did not attain space charge limited or even transitional behavior.

3.4   Conclusion

Nanoscale devices designed to isolate effects of gap distance and field enhancement were fabricated and test to study emission current and observe Fowler-Nordheim, Mott-Gurney, and Child-Langmuir behavior. The geometry of the devices was constructed such that a parallel plate device was fabricated with a protrusion into the gap that served to alter local field enhancement, though varying degrees of tip sharpness. The devices were made of gold and Titanium layered onto silicon wafers electrically isolated with SiO$_2$. Electrical tests similar to reverse bias diode testing was conducted, applying voltage to the side of the device with the protrusion and measuring the leakage current across the nanoscale gap of the device. A Signatone H-150W DC probe station was utilized to place tungsten PTT 12/4-25 needle probes with tips of 1.2 μm. The probes were placed using the stations microscope and micromanipulators on each of the gold test pads that were fabricated on the devices. The positive probe was always placed on the pad with the protrusion feature for each test. The test consisted of a voltage sweep starting at 0 V with steps of 0.005 V lasting 0.1 s until a spike in current was observed indicating the device had failed and was now

melted. Current was sampled at a rate of 10 samples per second. Device failure was confirmed under the microscope by observing the test pad degradation due to melting. Current (amperes) and voltage (volts) data was collected during the test and plotted with different fits and axis scaling to observe regions that are linear. The only observable linear trends were with certain portions of the FN curve. Figure 3.5 shows that $d_{eff} = d - h$ has a dominant effect on the emission current and breakdown of the device. The breakdown voltage increased with increasing gap size, as expected, while the protrusion width does not appear to have any effect on the emission current. This process was repeated for CL and MG scaling with similar results showing no effect of protrusion width. Emission area and mobility were estimated by using linear regression fits to the data and utilizing the theory from Darr, *et al.* to find a full solution to match the data. For $d_{eff} = 125$ nm $\pm$ 10 nm and a fitted emission area of 64 nm^2 with mobilities of (a) 0.0003 m^{2}V^{-1}s^{-1} and (b) 0.001 m^{2}V^{-1}s^{-1}; the transition region between field emission and space charge emission was evident, as noted previously in published work by Darr, *et al.* However, this transition was not observed for $d_{eff} = 28$ nm $\pm$ 10 nm and 450 nm $\pm$ 10 nm due to a local minimum being predicted by (3.5) and (3.6) implying that the mid-sized gaps more easily enter a space charge influenced transitional regime due to the effects of gap distance d_{eff}.

This chapter showed for the first time that while microscale gaps undergo field emission driven breakdown, nanoscale gaps may undergo breakdown either from field emission or directly from space-charge limited emission. Interestingly, the results were not monotonic with increasing gap distance since the smallest (28 nm) and largest (450 nm) gaps underwent breakdown from field emission, while the intermediate gap exhibited space charge effects (125 nm) prior to undergoing breakdown. Previous theory estimated that the asymptotic solutions for MG, FN, and CL intersected for a gap distance of 250 nm at atmospheric pressure. In reality (both experimentally and theoretically), such a condition will not exist since the conditions requiring this intersection do not, strictly speaking, satisfy each asymptotic solution; however, it serves as a signpost for a design parameters space where emission becomes sensitive to small perturbations in device conditions and parameters such as pressure, field enhancement, and general electrode conditions. These experiments demonstrate the design and construction of nanoscale devices to study electron emission and gas breakdown. Future studies can better characterize mobility to better describe the transition in emission regimes observed both experimentally and theoretically.

Future work will also consider the implications of pressure and temperature on these transitions, as well as the relevance of thermionic emission when heating is considered[76].